17 (2025) 100509

Contents lists available at ScienceDirect

Carbon Capture Science & Technology

journal homepage: www.elsevier.com/locate/ccst

Full Length Article

Feasibility assessment of a spray tower for gas-liquid reactive precipitation in CO_2 capture

Robert Kiefel [a], Jonas Görtz [a], Jan Haß [a], Julius Walorski [a], Falk Zimmer [a], Andreas Jupke [a,b,*]

[a] Fluid Process Engineering (AVT.FVT), RWTH Aachen University, 52074, Aachen, Germany
[b] Institute for Bio- and Geosciences (IBG-2), Forschungszentrum Jülich GmbH, 52428, Jülich, Germany

ARTICLE INFO

Keywords:
bis(iminoguanidine)
Rayleigh breakup
Spray tower
Precipitation
Crystallization
Carbon capture

ABSTRACT

The industrial deployment of CO_2 capture technologies for purifying gases with low CO_2 partial pressure (e.g., flue gas) has been limited due to substantial economic hurdles. Process intensification offers a pathway to enhance the cost efficiency of CO_2 sequestration. One approach that has garnered significant attention is the process integration of phase-change absorbents. Among these, bis(iminoguanidines) have shown considerable promise in recent literature. Particularly, glyoxal-bis(iminoguanidine) (GBIG) has demonstrated the ability to precipitate HCO_3^- with low regeneration energy demand. However, GBIG and comparable phase-change absorbents require the integration of alkaline scrubbing with reactive precipitation in a single unit operation (gas-liquid reactive precipitation), introducing operational challenges such as scaling and clogging in conventionally applied packed-bed columns. To mitigate these issues, this study investigates the use of a spray tower as a gas-liquid reactive precipitator for CO_2 capture from a flue gas surrogate. A pilot-scale spray tower is designed, constructed, and operated. Contrary to expectations, Rayleigh breakup of liquid jets induces a bimodal droplet size distribution in the lower sections of the tower, indicating limited scalability and highlighting the need for liquid recycling. For comparative purposes, the investigation includes a CO_3^{2-}-precipitating system ($Ba(OH)_2$) and a non-precipitating system (NaOH), alongside GBIG. All systems demonstrate stable operability in single-pass and batch modes. During liquid recycling, small amounts of solids are entrained to the tower top. Nevertheless, no evidence of scaling or clogging is detected at the orifice plate, suggesting that the precipitated solids are significantly smaller than the orifice diameter. In the final performance comparison, the GBIG system demonstrates superior CO_2 capture efficiency relative to the $Ba(OH)_2$ system. However, achieving this efficiency comes at the expense of process kinetics.

1. Introduction

Technologies for capturing CO_2 are widely acknowledged as vital tools in combating global greenhouse gas emissions (≈ 38 Gt in 2023 (Global Carbon Project, 2025)) (IPCC, 2022; Khan et al., 2023; Spigarelli and Kawatra, 2013; Hekmatmehr et al., 2024). Despite their importance, widespread industrial adoption has been limited, primarily due to economic barriers, especially concerning gas streams that contain CO_2 at moderate to low partial pressures, such as flue gas (Mumford et al., 2015). To enhance the commercial viability of CO_2 capture, process intensification can be considered a key strategy. In this context, phase-change absorbents have received increasing attention in recent studies (Zhang et al., 2019; Ochedi et al., 2021) and are also central to the present work.

In typical absorption-based systems, CO_2 is removed from the gas phase through chemical reactions such as hydration, hydroxylation or carbamate formation (McCann et al., 2009), all driven by the alkaline nature of the solvent. CO_2 release and sorbent regeneration are often carried out thermally (pH-T swing process) (Spigarelli and Kawatra, 2013). Consequently, sensible and latent heat losses to the solvent (e.g., H_2O) can not be avoided. To reduce these thermal inefficiencies, some process variants opt to precipitate CO_2-equivalent species after absorption (Darde et al., 2009; Kozak et al., 2009; Smith et al., 2017; Chen et al., 2008; Chen and Zhuo, 2020). This allows thermal energy to be applied directly to the CO_2-rich solids rather than to the entire liquid phase, thereby reducing energy losses. Although it is desirable to spatially separate alkaline scrubbing and reactive precipitation (Keith et al., 2018; Baciocchi et al., 2006), the integration into a single plant unit (gas-liquid reactive precipitation) may become necessary when employing a

* Corresponding author.
E-mail address: andreas.jupke@avt.rwth-aachen.de (A. Jupke).

https://doi.org/10.1016/j.ccst.2025.100509
Received 23 July 2025; Received in revised form 2 September 2025; Accepted 4 September 2025
Available online 8 September 2025

Abbreviations

CCDC	Cambridge Crystallographic Data Centre
CSD	Cambridge Structural Database
DAC	direct air capture
FGD	flue gas desulfurization
GBIG	glyoxal-bis(iminoguanidine)
GSD	geometric standard deviation
PTV	particle tracking velocimetry
PXRD	powder X-ray diffraction
SLPM	standard liter per minute
SMD	Sauter mean diameter

Dimensionless numbers

We	Weber number

Latin symbols

a	activity
c	concentration
$d_{orifice}$	diameter of the orifice
K	equilibrium constant
n	molar quantity
p	static pressure
$r_{1,min/max}$	radial boundaries for droplet identification
$r_{2,max}$	maximal displacement from a droplet's predicted position
S	solubility
$s_{droplet}$	maximal relative size deviation between corresponding droplets
T	temperature
$v_{droplet,50}$	median droplet velocity
v_{jet}	jet velocity
x_{box}	width of bounding box
y_{box}	height of bounding box

Greek symbols

κ	electrical conductivity
ξ	CO_2 recovery
ρ	density
σ_{liquid}	surface tension
ϕ	volume fraction
ψ	CO_2 capture efficiency
$\omega_{OH^-_{(eq)}}$	$OH^-_{(eq)}$ utilization efficiency

Subscripts

eq	equivalents
r	reaction index

phase-change absorbent. These systems form a second phase in response to CO_2 loading or temperature variation. A general classification can be made by their biphasic state (solid-liquid vs. liquid-liquid), solvent type (aqueous vs. non-aqueous), and the mechanism triggering second-phase formation (chemical or thermal) (Zhang et al., 2019; Ochedi et al., 2021). A novel class of aqueous, chemically responsive phase-change absorbents has shown promise: bis(iminoguanidines). Among these, aqueous glyoxal-bis(iminoguanidine) (GBIG) has garnered attention due to its ability to form crystals via hydrogen bonding of HCO_3^--dimers (cf. Fig. 1), which subsequently release CO_2 under mild heating with low regeneration energy demand (152 kJ $mol^{-1}_{CO_2}$ compared to 198 kJ $mol^{-1}_{CO_2}$ using aqueous monoethanolamine) (Williams et al., 2019; Custelcean et al., 2020). By precipitating as a sparingly soluble HCO_3^--salt, it doubles the molar absorption capacity for CO_2 compared to a CO_3^{2-}-salt. Although promising, GBIG is not viable for industrial application due to the low solubility of its non-protonated form (cf. Section 2.2). Nevertheless, it serves as model compound in this study for phase-change absorbents whose HCO_3^--salt exhibits low solubility. Given that guanidine-derived absorbents represent an emerging research area (Williams et al., 2019; Custelcean et al., 2020; Custelcean, 2021; Garrabrant et al., 2019), future investigations may prioritize the development of aqueous analogs with improved performance profiles.

Yet, a gas-liquid reactive precipitation process, as required for an aqueous GBIG system, involves managing solid formation during CO_2 absorption, which introduces challenges such as scaling and clogging. Due to these issues, traditional packed-bed columns appear unsuitable for such applications. Alternative reactor types better equipped to handle solids are bubble columns and spray towers. Although bubble columns have been widely investigated for reactive CO_2 precipitation (Chen et al., 2008; Chen and Zhuo, 2020; Chen et al., 2002, 2014b; Chen and Yu, 2018; Shim et al., 2016; Tamura and Tsuge, 2006; Varma et al., 2011; Maharloo et al., 2017), a considerable pressure drop in the gas phase is to be expected. This drawback becomes critical when dealing with feed gases containing CO_2 at low to moderate partial pressures, where the required volumetric flow rates are high. In contrast, spray towers offer a low pressure drop (Koller et al., 2011; Javed et al., 2010), making them a potentially attractive option. However, their application in gas-liquid reactive precipitation for CO_2 capture has been sparsely reported in the literature (Perry et al., 2012; Westendorf et al., 2010; Onimisi et al., 2016; Wu et al., 2018). Perry et al. (2012) and Westendorf et al. (2010) employ a non-aqueous aminosilicone-based absorbent in a spray reactor to precipitate a carbamate salt during CO_2 separation from a simulated flue gas stream. In other studies, Onimisi et al. (2016) and Wu et al. (2018) explore the spray-induced precipitation of $CaCO_3$ using $Ca(OH)_2$ slurries or solutions. However, these investigations primarily focus on proof-of-concept, precipitate characterization, and *in situ* reaction monitoring, without addressing practical operability. Other sources (Sanchez-Fernandez et al., 2013; Raksajati et al., 2016; van der Ham et al., 2016) have acknowledged the need for spray towers in gas-liquid reactive precipitation, yet practical evaluations of their operability remain limited. Beyond CO_2 capture, spray towers are industrially established for flue gas desulfurization (FGD), especially in coal-fired power plants, where lime or limestone slurries are used to remove SO_2 by forming solid $CaSO_3$ and/or salable $CaSO_4$ (gypsum) (Srivastava and Jozewicz, 2001; Bandyopadhyay and Biswas, 2007; Zhu et al., 2015; Buecker, 2008). Additionally, ongoing research explores solid-liquid-gas reaction systems in spray towers, including mineralization of industrial waste products like carbide slag (Liu et al., 2024; Wang et al., 2025). The common feature across all these applications is the reliance on spray towers due to their ability to handle high gas flow rates with low pressure drop, while simultaneously enabling *in situ* formation and transport of solids.

This study is the first to explicitly investigate the practical operability of spray towers for gas-liquid reactive precipitation in CO_2 capture. The thermodynamic and kinetic basis of the liquid-phase reaction system is first reviewed to facilitate the analysis of system behavior. To explore the spray tower, a pilot-scale plant is designed, constructed, and tested experimentally. Prior to gas-liquid reactive precipitation, the uniformity of droplet size and velocity along the tower height is investigated to evaluate scalability and the need for liquid recycling. Afterward, the operability of the spray tower as a gas-liquid reactive precipitator with slurry recycling is assessed. Finally, the CO_2 capture performance is quantitatively examined. Although this work focuses on an aqueous GBIG solution, a CO_3^{2-}-precipitating system ($Ba(OH)_2$) and a non-precipitating system (NaOH) are included in the study to enable a comparative evaluation.

2. Fundamentals

2.1. Thermodynamics and kinetics of CO_2 reactive absorption

To assess the CO_2 capture performance, the thermodynamics and kinetics of the liquid-phase reaction system are analyzed below. The

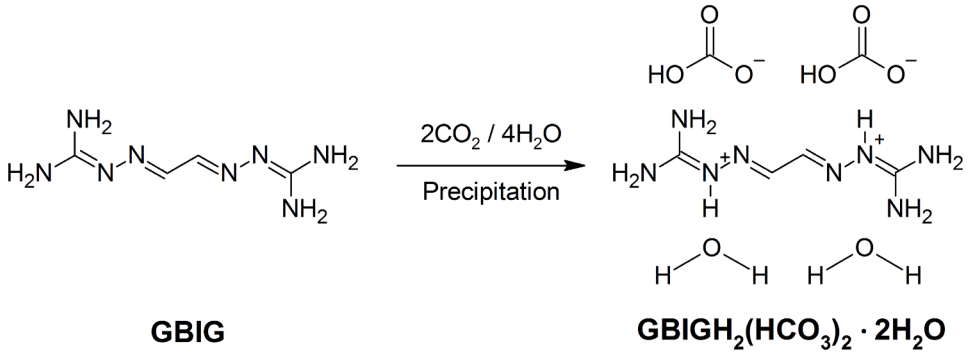

Fig. 1. CO_2 capture with aqueous GBIG (Derived from Williams et al., 2019 and Custelcean et al., 2020).

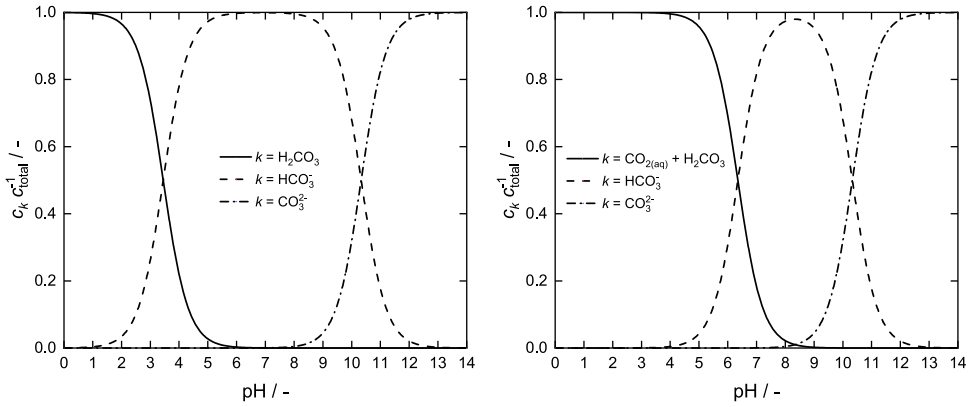

(a) Dissociative species distribution at equilibrium

(b) Apparent species distribution at equilibrium

Fig. 2. pH-dependent CO_2 dissociation in aqueous systems at 25°C.

reactive absorption of CO_2 into an aqueous medium involves the physical dissolution followed by either hydration to H_2CO_3 or hydroxylation to HCO_3^-. These reactions are accompanied by two dissociation equilibria of carbonate species and the self-ionization of H_2O. The liquid phase reaction network (Kordac and Linek, 2008; Wang et al., 2010) is represented by

$$CO_{2(aq)} + H_2O \rightleftharpoons H_2CO_3, \tag{R1}$$

$$H_2CO_3 \rightleftharpoons H^+ + HCO_3^-, \tag{R2}$$

$$HCO_3^- \rightleftharpoons H^+ + CO_3^{2-}, \tag{R3}$$

$$H_2O \rightleftharpoons H^+ + OH^- \text{ and} \tag{R4}$$

$$CO_{2(aq)} + OH^- \rightleftharpoons HCO_3^-. \tag{R5}$$

A general modeling framework for aqueous phase reactions described in the supplementary material (cf. Appendix A) is used to analyze the equilibria and kinetics of the present system.

The equilibrium expression for the CO_2 hydration reaction (R1) is given by

$$K_{R1} = \frac{a_{H_2CO_3}}{a_{CO_{2(aq)}} \cdot a_{H_2O}} \approx K_{c,R1} = \frac{c_{H_2CO_3}}{c_{CO_{2(aq)}}}, \tag{1}$$

where $K_{c,R1}(25°)$ of 1.26×10^{-3} to 1.70×10^{-3} can be derived from the literature (Wang et al., 2010; Adamczyk et al., 2009; Housecroft and Sharpe, 2012). The equilibria for the subsequent dissociation reactions (R2) and (R3) are characterized by their respective acid dissociation constant. Reported $pK_{R2}(25°C)$ values for the first dissociation step range between 3.45 and 3.70 (Wang et al., 2010; Adamczyk et al., 2009; Housecroft and Sharpe, 2012), while the second dissociation step has a $pK_{R3}(25°C)$ of 10.33 (Harned and Scholes Jr, 1941; Lide, 2004). The self-ionization of H_2O is described by a $pK_{R4}(25°C)$ of 14 (Lide, 2004; Gmehling et al., 2019). Together, these dissociation reactions (R2)–(R4) govern the pH-dependent species distribution at equilibrium, as illustrated in Fig. 2(a). Notably, Reaction (R1) tends to favor $CO_{2(aq)}$ over H_2CO_3, thereby creating a relative depletion of carbonate species, especially at lower pH (Crovetto, 1991; Mook, 2000). To reflect this behavior within the conventional pH-dependent dissociation schematic, the concentrations of $CO_{2(aq)}$ and H_2CO_3 are combined into a single lumped species and an apparent equilibrium constant is introduced as follows (Mook, 2000; Soli and Byrne, 2002):

$$K_{c,R1/R2,app} = \frac{c_{H^+} \cdot c_{HCO_3^-}}{c_{CO_{2(aq)}} + c_{H_2CO_3}} = \frac{K_{c,R1}}{1 + K_{c,R1}} \cdot K_{c,R2} \approx K_{R1/R2,app}. \tag{2}$$

Multiple sources report a value of 6.35 for $pK_{R1/R2,app}(25°C)$ (Adamczyk et al., 2009; Lide, 2004; Mook, 2000). This apparent equilibrium behavior is illustrated in Fig. 2(b). In contrast to the dissociative species distribution, the apparent distribution corresponds to experimental observations from titration curves of aqueous carbonate systems (Adamczyk et al., 2009). Despite similar values (Harned and Davis Jr, 1943), $K_{R1/R2,app}$ should not be conflated with $K_{R1/R2}$. The latter is commonly used in process modeling software, such as Aspen Plus®, and typically described by

$$K_{R1/R2} = \frac{a_{H^+} \cdot a_{HCO_3^-}}{a_{CO_{2(aq)}} \cdot a_{H_2O}} = K_{R1} \cdot K_{R2} \approx \frac{c_{H^+} \cdot c_{HCO_3^-}}{c_{CO_{2(aq)}}} = K_{c,R1} \cdot K_{c,R2} = K_{c,R1/R2}. \tag{3}$$

Alongside the hydration of $CO_{2(aq)}$, the hydroxylation pathway (R5) proceeds in parallel. These two reaction routes are interlinked through

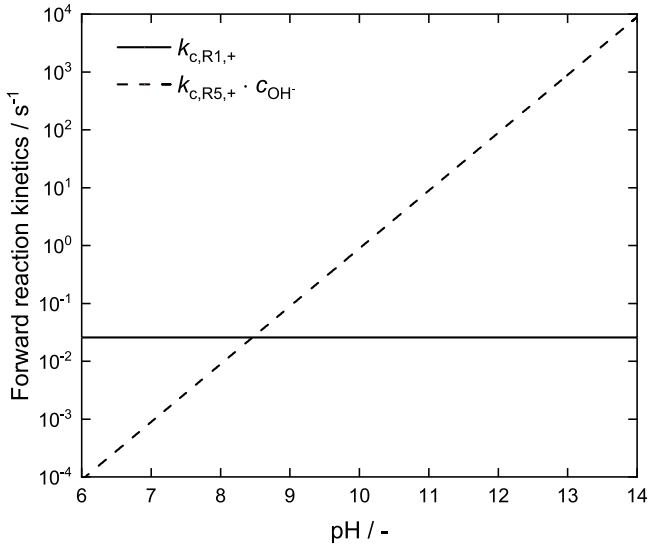

Fig. 3. Forward kinetic parameters of (R1) and (R5) with respect to the solution's pH at 25°C.

the dissociation of H_2CO_3 (R2) and the self-ionization of H_2O (R4). The corresponding equilibrium constant governing this coupled system is defined by

$$K_{R5} = \frac{a_{HCO_3^-}}{a_{CO_{2(aq)}} \cdot a_{OH^-}} = \frac{K_{R2}}{K_{R4}} \cdot K_{R1}, \tag{4}$$

where $K_{R5}(25°C)$ can be derived from the literature ranging from 4.23×10^7 to 4.43×10^7 (Wang et al., 2010; Adamczyk et al., 2009; Housecroft and Sharpe, 2012).

The distinction between dissociative and apparent equilibrium representations of the pH-dependent species distribution (cf. Fig. 2) is critical for the kinetic analysis of the system. While the dissociation reactions (R2)–(R4) are generally assumed to attain equilibrium instantaneously, the hydration and hydroxylation reactions proceed at discernible kinetics (McCann et al., 2009; Wang et al., 2010; Pinsent et al., 1956; Hill, 2006). Consequently, a dissociative pseudo-equilibrium (cf. Fig. 2(a)) can be assumed to persist permanently, while the hydration and hydroxylation reactions control the overall kinetics. The dominant kinetic pathway between these two reactions depends on the system's pH (Pinsent and Roughton, 1951). The forward rate constant for the hydration reaction, $k_{c,R1,+}(25°C)$, lies between $17.54\,s^{-1}$ and $24.80\,s^{-1}$, and is formally independent of the pH (Wang et al., 2010; Pinsent et al., 1956; Pocker and Bjorkquist, 1977; Ho and Sturtevant, 1963). In contrast, the forward rate constant for the hydroxylation reaction, $k_{c,R5,+}(25°C)$, is pH-dependent and reported between $6\times10^3\,L\,mol^{-1}\,s^{-1}$ and $12\times10^3\,L\,mol^{-1}\,s^{-1}$ (Wang et al., 2010; Pinsent et al., 1956; Pocker and Bjorkquist, 1977; Ho and Sturtevant, 1963; Sirs, 1958). Fig. 3 illustrates the forward kinetics of both reactions as a function of pH, assuming a fixed $k_{c,R5,+}(25°C)$. It can be inferred that hydroxylation overtakes hydration as the primary conversion mechanism for $CO_{2(aq)}$ as the pH exceeds ≈ 8.5.

2.2. Selection of absorbent systems

GBIG is identified as appropriate absorbent system as it forms sparingly soluble HCO_3^--salts ($S_{GBIGH_2(HCO_3)_2\cdot2H_2O}(25°C) = 0.0072\,mol\,L^{-1}$) with low regeneration energy demand (Williams et al., 2019; Custelcean et al., 2020). Although the low solubility of its non-protonated form ($S_{GBIG}(25°C) = 0.0115\,mol\,L^{-1}$) limits the overall uptake capacity (Williams et al., 2019), this study employs GBIG as a model compound for HCO_3^--precipitating phase-change absorbents. Notably, $GBIGH_2^{2+}$ undergoes the following two dissociation reactions:

$$GBIGH_2^{2+} \rightleftharpoons GBIGH^+ + H^+ \text{ and} \tag{R6}$$

$$GBIGH^+ \rightleftharpoons GBIG + H^+. \tag{R7}$$

The acid dissociation equilibria for these reactions are characterized by pK values of 7.33 and 8.65 at 25°C, respectively (Williams et al., 2019) (cf. Appendix B for an illustration of the pH-dependent dissociation behavior). These values suggest that GBIG displays only mild alkalinity, even more moderate than that of common amines or amino acids when dissolved in aqueous solution (Zhang et al., 2018).

An alkaline earth metal is chosen for CO_3^{2-} precipitation as these cations do not form solid HCO_3^- species. In CO_2 capture, alkaline earth metals are commonly employed in processes integrating alkaline scrubbing, causticization and calcination for direct air capture (DAC) (Keith et al., 2018; Baciocchi et al., 2006). For the present study, Ba^{2+} is employed as the precipitating agent, as it exhibits the largest solubility gradient between its hydroxide and carbonate salts among the alkaline earth metals ($S_{Ba(OH)_2}(25°C) = 0.287\,mol\,kg_{H_2O}^{-1}$ and $S_{BaCO_3}(20°C) = 7\times10^{-5}\,mol\,kg_{H_2O}^{-1}$ (Lide, 2004)).

Aqueous NaOH is used as a non-precipitating reference. This alkaline solution is frequently used in comparative studies of various alkaline scrubbers (Chen et al., 2014a; Green and Southard, 2019; Aroonwilas and Tontiwachwuthikul, 1997; Li et al., 2019).

No additional buffers are added to the systems. Consequently, the chemical species responsible for inducing precipitation also supplies the necessary alkalinity.

2.3. Droplet formation mechanism

To control droplet size and velocity, the droplet formation mechanism needs to be understood. When liquid flows slowly from an orifice into a continuous gas phase, sizable droplets form and detach at regular intervals. This behavior is known as the dripping regime. However, if the discharge velocity surpasses a critical value, the flow transitions into a liquid jet. This transition is commonly characterized using the Weber number (We_{liquid}) at the orifice outlet, which is defined by

$$We_{liquid} = \frac{\rho_{liquid} \cdot v_{jet}^2 \cdot d_{orifice}}{\sigma_{liquid}}, \tag{5}$$

where ρ_{liquid} is the density of the liquid, v_{jet} is the jetting velocity, $d_{orifice}$ is the diameter of the orifice and σ_{liquid} is the surface tension of the liquid. The Weber number expresses the ratio of inertial to surface tension forces. When it exceeds a critical range, typically between 2 and 8, a continuous jet forms and eventually breaks up into a sequence of droplets (Van Hoeve et al., 2010; Lin and Reitz, 1998; Suñol and González-Cinca, 2015).

The injection of a liquid into a stagnant gas environment can be classified into four distinct jet breakup regimes: Rayleigh breakup regime, first wind-induced regime, second wind-induced regime and atomization regime. These regimes are illustrated in Fig. 4, arranged according to increasing jet velocity. In the Rayleigh breakup regime, an increase in jet velocity corresponds to a longer breakup length, defined as the distance from the orifice to the location at which the liquid jet disintegrates. In contrast, the first wind-induced regime exhibits a reduction in this breakup length as jet velocity rises. Both of these regimes typically produce droplets comparable in size to the jet diameter. As the system transitions into the second wind-induced regime, the breakup point shifts closer to the nozzle. In the atomization regime, fragmentation of the liquid occurs immediately at the orifice. Notably, both the second wind-induced and atomization regimes produce significantly smaller droplets than the original jet diameter (Lin and Reitz, 1998; Kim and Song, 2019).

According to Cho et al. (2018), enhancing the uniformity of spatial droplet distribution, droplet size, droplet velocity and gas velocity

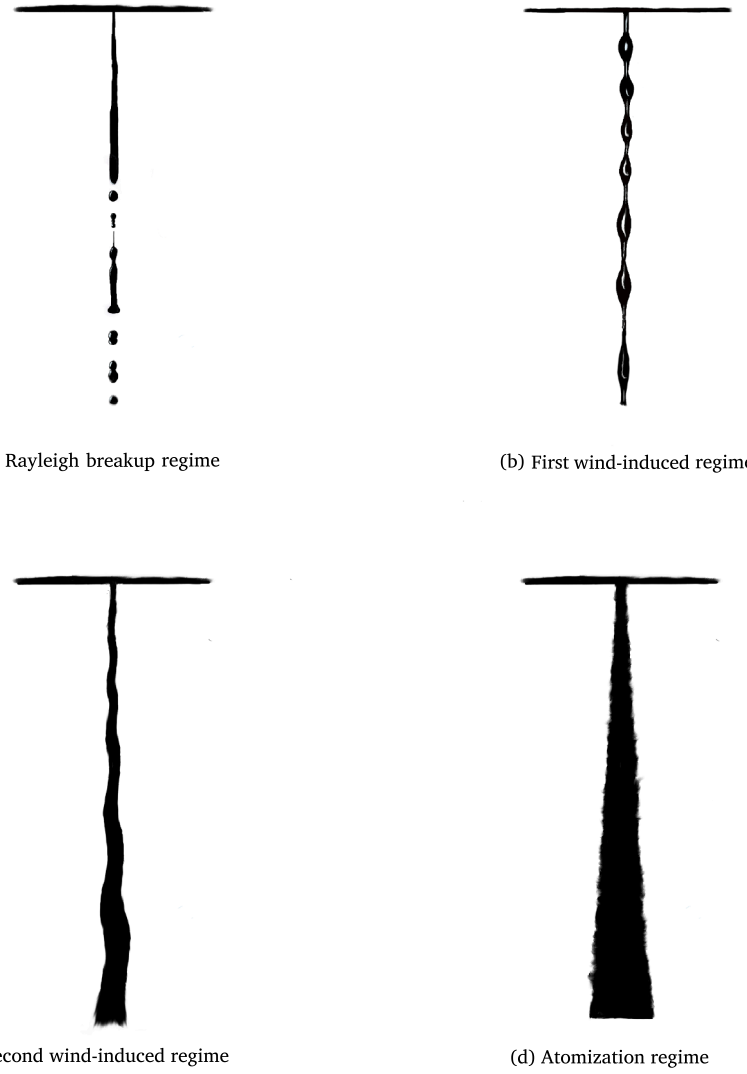

(a) Rayleigh breakup regime

(b) First wind-induced regime

(c) Second wind-induced regime

(d) Atomization regime

Fig. 4. Schematic illustration of liquid jet breakup classified by regime type (redrawn from Lin and Reitz, 1998).

leads to significant improvements in CO_2 recovery. In practical applications, spray nozzles are often employed that disperse liquid into a conical mist through atomization (Javed et al., 2010; Perry et al., 2012; Li et al., 2019; Lim et al., 2013; Stolaroff et al., 2008). However, this approach often results in pronounced nonuniformities, which diminish the available interfacial area for mass transfer due to droplet-droplet and droplet-wall collisions. Moreover, smaller droplets are susceptible to entrainment by the gas stream, leading to further performance deterioration (Javed et al., 2010; Cho et al., 2018).

This study specifically focuses on operating within the Rayleigh breakup regime, which forms vertically aligned droplets that exhibit low variation in size and velocity (Cho et al., 2018). An additional advantage of this regime is its relative insensitivity to changes in jet velocity or pressure above the orifice plate (Van Hoeve et al., 2010; Suñol and González-Cinca, 2015; Tyler, 1933). Only as the inertial force exerted by the surrounding gas approaches the magnitude of the surface tension force, the transition into the first wind-induced regime is induced. The onset of this regime is typically identified using the gas Weber number (We_{gas}), given by

$$We_{gas} = \frac{\rho_{gas}}{\rho_{liquid}} \cdot We_{liquid}. \tag{6}$$

The threshold for the first wind-induced regime is characterized by a We_{gas} in the range of 0.2 to 0.4 (Van Hoeve et al., 2010; Lin and Reitz, 1998).

3. Materials and methods

3.1. Performance metrics

To ensure a consistent performance comparison between the component systems examined in this study, the following definitions are introduced:

$$\xi = \frac{n_{liquid+solid,out,CO_{2(eq)}}}{n_{gas,in,CO_2}}, \tag{7}$$

$$\psi = \frac{n_{liquid+solid,out,CO_{2(eq)}}}{n_{liquid,in,OH^-_{(eq)}} - n_{liquid,out,OH^-_{(eq)}}} \text{ and} \tag{8}$$

$$\omega_{OH^-_{(eq)}} = \frac{n_{liquid,in,OH^-_{(eq)}} - n_{liquid,out,OH^-_{(eq)}}}{n_{liquid,in,OH^-_{(eq)}}}, \tag{9}$$

where ξ is the CO_2 recovery, ψ is the CO_2 capture efficiency and $\omega_{OH^-_{(eq)}}$ is the $OH^-_{(eq)}$ utilization efficiency. The term $n_{CO_{2(eq)}}$ represents the total

quantity of CO_2 equivalents, given by

$$n_{CO_{2(eq)}} = n_{CO_{2(aq)}} + n_{H_2CO_3} + n_{HCO_3^-} + n_{CO_3^{2-}}. \quad (10)$$

Correspondingly, $n_{OH^-_{(eq)}}$ specifies the amount of OH^- equivalents that are capable of deprotonating H_2CO_3, defined as

$$n_{OH^-_{(eq)}} = n_{OH^-} + 2 \cdot n_{GBIG}. \quad (11)$$

3.2. Preparation of feed solutions

In all absorption experiments, feed solutions contain an $OH^-_{(eq)}$ concentration of $0.05\,mol\,L^{-1}$. Consequently, the NaOH solution is prepared at a concentration of $0.05\,mol\,L^{-1}$, whereas the $Ba(OH)_2$ solution is adjusted to $0.025\,mol\,L^{-1}$. However, a $0.025\,mol\,L^{-1}$ solution of GBIG is not viable due to its limited aqueous solubility ($S_{GBIG}(25°C) = 0.0115\,mol\,L^{-1}$ Williams et al., 2019). To overcome this constraint, a mixed solution is employed consisting of $0.05\,mol\,L^{-1}$ GBIG and an equal concentration of HCl. This formulation ensures that the $OH^-_{(eq)}$ capacity remains at $0.05\,mol\,L^{-1}$, while the nonprotonated GBIG concentration is held below its solubility.

The solid reagents are dissolved in distilled H_2O using magnetic stirring for a minimum of 12 h under an inert N_2 atmosphere. Anhydrous NaOH pellets (≥ 98 %) and $Ba(OH)_2 \cdot 8H_2O$ powder (≥ 98 %) are acquired from Sigma-Aldrich Chemie GmbH (Germany) and Carl Roth GmbH + Co. KG (Germany), respectively. According to the supplier's certificate of analysis, the $Ba(OH)_2 \cdot 8H_2O$ powder contains approximately ≤ 1.0 % $BaCO_3$, which is sparingly soluble. Therefore, following dissolution of $Ba(OH)_2 \cdot 8H_2O$, any undissolved material is removed via filtration. GBIG is synthesized following the procedure detailed in the supplementary material (cf. Appendix C). To confirm the $OH^-_{(eq)}$ capacity of the prepared solutions, acid-base titration is conducted as described in Section 3.6. Notably, while the initial pH of the GBIG solution is ≈ 8, the pH of the NaOH and $Ba(OH)_2$ solutions ranges between 12.5 and 13.

3.3. Experimental setup

Fig. 5 presents a three-dimensional rendering of the constructed spray tower. The vertical section serving as the gas-liquid contacting zone is fabricated from polymethyl methacrylate, designed with an inner diameter of 32 mm and a height of ≈ 1.2 m. The connecting components, including flat gaskets, o-rings and flanges are made from ethylene propylene diene monomer rubber, acrylonitrile butadiene rubber and polypropylene, respectively. For a detailed illustration of the spray tower within the experimental setup, refer to the supplementary material (cf. Appendix D).

To evaluate the behavior of the three component systems, two distinct experimental procedures are employed. Initially, each alkaline solution is circulated through the spray tower in a batch mode, with the cycle repeated until the system reaches steady-state conditions. This approach allows to determine system states after the $OH^-_{(eq)}$ capacity in the liquid phase is fully consumed. The resulting data reflect the maximum CO_2 capture capacity for each system, effectively representing the absorption equilibrium under the given input streams. Following this, single-pass experiments are performed. These experiments allow for a comparative analysis of the absorbent systems' kinetic performances under stationary process conditions.

Fig. 6 depicts the process diagram for the spray tower system. The alkaline solvent is supplied by a peristaltic pump (Masterflex™ L/S™ computer-compatible digital drive combined with an Easy-Load™ II pump head, purchased from Cole-Parmer GmbH (Germany)). In batch mode, the solution is drawn from the sump, while in single-pass mode, it is supplied from a separate reservoir. In both cases, the fluid is fed into a pressure-backed tank before being introduced into the spray head. Maintaining a stable liquid level within the pressure-backed tank ensures that the flow delivered to the spray tower matches the output

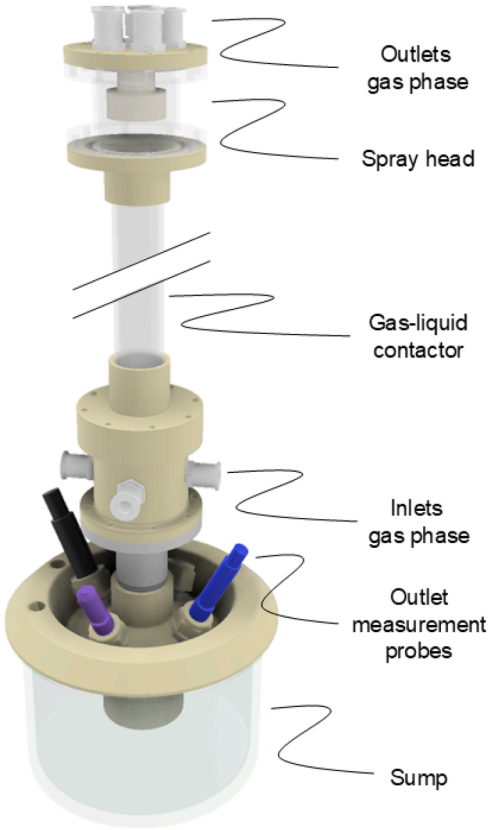

Fig. 5. 3D model of the spray tower.

from the pump. This setup avoids flow pulsations typically associated with peristaltic pumps, thereby preserving consistent droplet formation. The spray head is installed at the top of the tower's gas-liquid contacting zone and is designed to distribute droplets evenly across the entire cross-section. A distribution plate with 43 orifices, each measuring 150 µm in diameter, disperses the alkaline solvent into fine droplets. The cavity below the tower ensures that droplets do not enter the gas inlets. These inlets are positioned just above the liquid level in the sump. High-purity gas streams are metered with Alicat MCP-50SLPM-D flow controllers, purchased from TrigasDM GmbH (Germany), and subsequently combined to form a flue gas surrogate consisting of 15 mol % CO_2 (grade 4.8) and 85 mol % N_2 (grade 5.0), resembling compositions employed in other CO_2 absorption studies (Mumford et al., 2015; Cho et al., 2018; Fosbøl et al., 2014). To reduce H_2O absorption within the tower, the gas mixture is humidified using distilled H_2O before entering the plant unit. Although this pre-humidification is likely omitted in industrial-scale processes, it is necessary in the current experimental context to prevent erroneous results due to drying out.

To monitor the behavior of the liquid phase throughout the experiments, pH and electrical conductivity (κ) are measured. The pH is recorded using pHenomenal® 221 probes, supplied by VWR International GmbH (Germany), paired with HND-R 106 measuring devices, acquired from Kobold Messring GmbH (Germany). κ is tracked using TetraCon®925 IDS conductivity cells connected to MultiLine® 3620 IDS digital multiparameter portable meters, also sourced from VWR International GmbH (Germany). These sensors are installed at the entries to the spray head and the sump. Conductivity measurements are used exclusively to verify that steady-state conditions are established. Additionally, pressure sensors GENSPEC GS4200, acquired from SUCO Robert Scheuffele GmbH & Co. KG (Germany), are installed at the liquid feed, gas inlet, and gas outlet. The gas composition at the outlet is continuously analyzed using a Vaisala CARBOCAP® CO_2 probe GMP251.

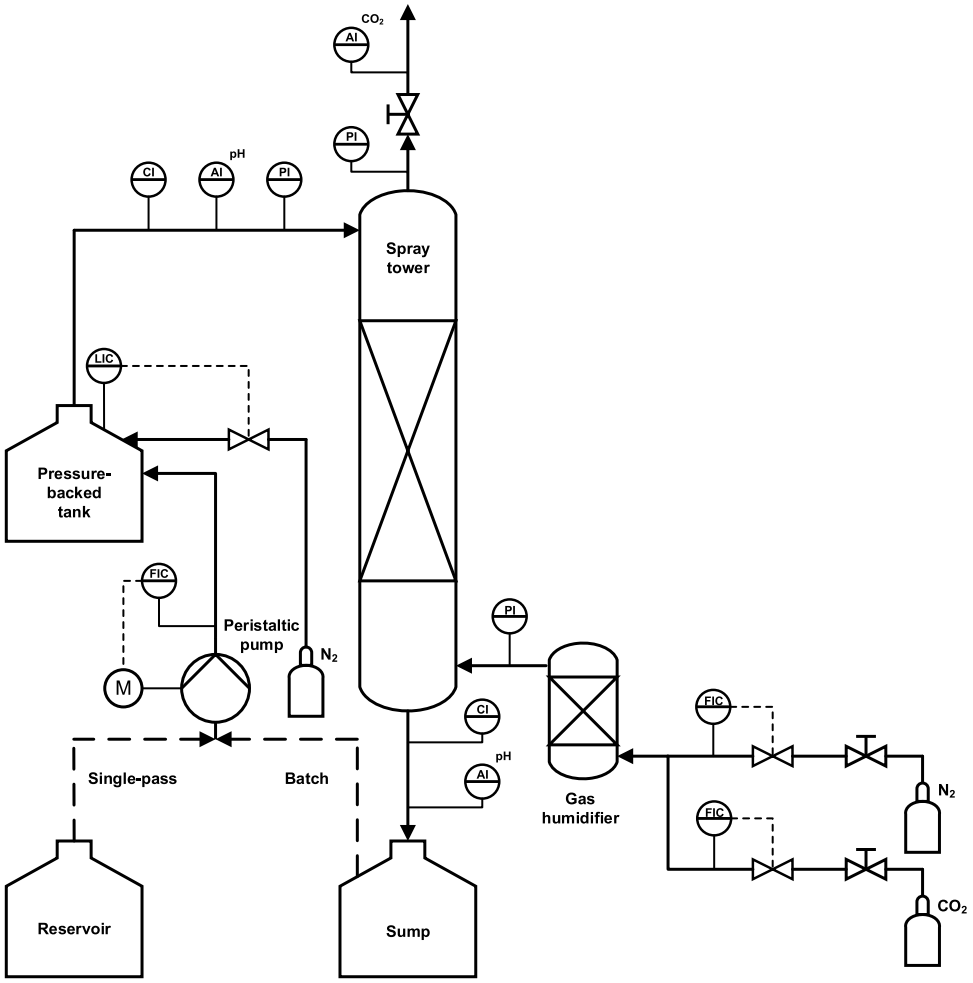

Fig. 6. Process flowsheet of experimental setup.

Controlled variables include the liquid and dry gas flow rate. Through a tailored LabVIEW interface the experimental setup is operated and monitored. Measurements from all sensors are logged every 6 s. Steady-state conditions are assumed when the electrical conductivity of the system remains constant for at least 15 min.

Across all trials, the liquid flow rate is kept constant at 144 mL min^{-1}, while the gas flow rate is varied between 0.5 SLPM and 8 SLPM. For the batch mode experiments, the gas flow rate is fixed at 2 SLPM. To prevent premature CO_2 uptake, the entire system is flushed with N_2 (grade 5.0) before each experiment.

With a constant liquid flow rate and the same orifice plate employed in all experiments, the Weber numbers for the liquid and gas phases can be estimated using the material properties of H_2O and an H_2O-saturated gas stream composed of 15 mol% CO_2 and 85 mol% N_2 at $T = 25°C$ and $p = 1$ bar. Under these conditions, We_{liquid} and We_{gas} are calculated to ≈ 20.73 and ≈ 0.03, respectively. These values suggest that the jet breakup behavior is governed by the Rayleigh regime under the given conditions.

3.4. Measurement of droplet size and velocity

To assess the uniformity of droplet size and velocity across the height of the spray tower, measurements are taken at the top, middle and bottom sections of the gas-liquid contacting zone. The method, initially developed for measuring gas bubble sizes (Görtz et al., 2024b) and velocities (Görtz et al., 2024a) in parallel plate electrolyzers, is adapted for droplet analysis in the present system. For this purpose, the spray tower is continuously fed with distilled H_2O. At each designated height, images of droplets are captured using a monochromatic high-speed camera XStream Mini model XSM 5K (5120 × 2880 pixels) from Imaging Solutions GmbH (Germany). The sensor, with a resolution of 3.5 px, is paired with a LM1119TC telecentric lens from Kowa Optimed Deutschland GmbH (Germany), which eliminates the need for additional calibration. Magnification is set to 0.95 x for the top section and 0.75 x for the middle and bottom sections, corresponding to pixel sizes of 3.7 µm and 4.7 µm, respectively. Frame rate and acquisition time vary, with the top section recorded at 2500 s^{-1} for 2 s, while the lower sections are acquired at 800 s^{-1} for 6.25 s. Illumination is provided by bar lights directed at the telecentric lens to increase brightness and improve edge definition by the use of a smaller aperture. The focal plane is positioned in the middle of the gas-liquid contacting zone, providing a depth of field between 300 µm and 450 µm. To reduce motion blur, the exposure time is configured to 31 µs.

In the collected images, droplets are identified using a publicly accessible implementation of the Mask region-based convolutional neural network (Mask R-CNN) along with its default weights (Sibirtsev, 2022; Sibirtsev et al., 2023, 2024). Each droplet identified in the image is encapsulated by a bounding box, defined by its width x_{box} and height y_{box}. To characterize the droplet size, the diameter is used and calculated following

$$d_{droplet} = \sqrt{x_{box} y_{box}}. \tag{12}$$

To ensure accurate droplet size measurements, constraints are imposed on the aspect ratio ($x_{box} y_{box}^{-1}$) and droplets intersecting the image boundary are excluded from analysis. Droplet velocity magnitude

($v_{droplet}$) is calculated using a two-dimensional, four-frame, forward-backward particle tracking velocimetry (PTV) algorithm, originally introduced by Vukasinovic et al. (2004) and tailored by Görtz et al. (2024a). For this study, the PTV algorithm has been implemented with a modified parameterization, as detailed in the supplementary material (cf. Appendix E).

3.5. Solid characterization

Powder X-ray diffraction (PXRD) analysis of the dried solids is conducted using a STADI-P diffractometer (STOE & Cie GmbH, Germany) in Guinier geometry. The setup utilizes Cu-Kα1-rays ($\lambda = 1.540\,59$ Å in combination with a Ge-monochromator (Johansson type)). Data acquisition is performed in 2θ increments of $0.015°$. Diffraction intensities are captured using an image plate detector (STOE IP-PSD). For measurement, the samples are evenly spread on a polyacetate foil at ambient temperature. To enhance the counting statistics of the intensity data, the samples are rotated throughout the scan.

PXRD patterns obtained from the experiments are evaluated against simulated diffractograms. The simulations are generated using Mercury (version 2024.3.1) supplied by the Cambridge Crystallographic Data Centre (CCDC). Three-dimensional molecular structures of the components are sourced from the Cambridge Structural Database (CSD). Database identifiers and deposition numbers are noted in the figure legends.

3.6. Species distribution analysis

Following each CO_2 capture experiment, the entire solution/slurry is collected in the sump of the spray tower and subsequently vacuum filtered (filter pore size 2.7 µm). The liquid volume is recorded and the solid fraction is dried at ambient conditions until its mass stabilizes. Vacuum drying should be avoided, as it may initiate sorbent regeneration, as described in the supplementary material (cf. Appendix F). Following drying, the weight of the solids is determined. The total concentration of HCO_3^- and CO_3^{2-} in the liquid phase is quantified using a Titrator Excellence T5 equipped with a DGi102-Mini pH probe (Mettler-Toledo GmbH, Germany). For this purpose, a sample of the liquid phase is titrated with a $0.1\,mol\,L^{-1}$ HCl solution obtained from Carl Roth GmbH + Co. KG (Germany).

To calculate the efficiency metrics presented in Section 3.1, it is necessary to determine the distribution of species within the liquid phase. For this purpose, the dissociation reactions (R2)–(R4) are assumed to attain equilibrium instantaneously (cf. Section 2.1). Therefore, at any time, the system can be characterized by the pH-dependent dissociative species distribution (cf. Fig. 2(a)). Additionally, dissolved salts are considered fully dissociated. To suppress inaccuracies arising from solid dissolution and dehydration reaction caused by the lower CO_2 partial pressure in air, filtration and titration of the solution are conducted immediately after the CO_2 capture experiment is finished. Using the outlined assumptions in conjunction with the acquired experimental measurements, the distribution of chemical species present in the liquid phase for each of the three component systems can be determined as described in the supplementary material (cf. Appendix G).

4. Results and discussion

4.1. Analysis of droplet size and velocity

During experimental spray tower operation, liquid jet breakup is successfully induced. Fig. 7(a) displays the droplet formation observed during a CO_2 capture experiment carried out in this study, closely resembling the appearance of a Rayleigh breakup regime (cf. Fig. 4(a)). The entire array of droplet streams emitted from the spray head is presented in Fig. 7(b).

Fig. 8 illustrates the droplet size distribution analyzed as a function of spray tower section and gas-to-liquid volume flow ratio ($\dot{V}_{gas,in}\dot{V}^{-1}_{liquid,in}$). Droplet diameters are grouped into intervals of 0.02 mm. Since the liquid flow rate remains constant throughout all experiments ($144\,mL\,min^{-1}$), gas flow rates of 0.5, 2, and 8 SLPM translate to $\dot{V}_{gas,in}\dot{V}^{-1}_{liquid,in}$-ratios of 3.8, 15.4, and 61.5, respectively. The figures also include the Sauter mean diameter (SMD) along with the geometric standard deviation (GSD).

As anticipated (cf. Section 2.3), the Rayleigh breakup of liquid jets produces a narrow droplet size distribution in the top section of the gas-liquid contacting zone, regardless of the $\dot{V}_{gas,in}\dot{V}^{-1}_{liquid,in}$-ratio. This observation is consistent with the findings of Cho et al. (2018), who also employ a perforated distributor plate to create a highly uniform droplet size distribution immediately following jet breakup. Their reported SMD (0.31 mm) closely matches the 0.27 mm found in the current study. Furthermore, their GSD of 1.2 is slightly larger than the value observed here (≈ 1.1). Notably, Cho et al. (2018) do not investigate the lower sections of the spray tower and assume the droplet size distribution to remain consistent throughout its height. However, Fig. 8 reveals a bimodal droplet size distribution in the middle section, with a markedly increased SMD of 0.45 mm compared to the top. Presumably, this is due to collisions among droplets of similar size. This trend seems unaffected by changes in the $\dot{V}_{gas,in}\dot{V}^{-1}_{liquid,in}$-ratio. In contrast, the bottom section's droplet size distribution is strongly influenced by the $\dot{V}_{gas,in}\dot{V}^{-1}_{liquid,in}$-ratio. At lower values, there is a significant rise in SMD from the middle to the bottom section, while at higher ratios, the increase is much less pronounced.

The analysis of droplet velocity supports the assumption of collision. Fig. 9 presents the median values as a function of vertical section and $\dot{V}_{gas,in}\dot{V}^{-1}_{liquid,in}$-ratio. In addition, these are provided for each droplet size class in the supplementary material (cf. Appendix H). Following jet disintegration, droplets exhibit velocities in the range of $2.7\,m\,s^{-1}$ to $2.8\,m\,s^{-1}$, which is lower than the superficial liquid velocity in the orifice ($3.2\,m\,s^{-1}$). As the droplets descend toward the middle section of the spray tower, they undergo additional deceleration, with their median speed decreasing to approximately $2.0\,m\,s^{-1}$, which corresponds to the size-dependent terminal velocity of H_2O droplets in air. (Holterman, 2003). It is hypothesized that the uneven deceleration of droplets after initial breakup enhances the frequency of droplet-droplet collisions, thereby broadening the droplet size distribution.

Overall, the initially narrow droplet size distribution formed immediately after jet breakup does not persist throughout the spray tower. A consistent increase in droplet size is observed, which can only be mitigated by increasing the $\dot{V}_{gas,in}\dot{V}^{-1}_{liquid,in}$-ratio. Furthermore, a bimodal size distribution emerges. As these spatial non-uniformities inhibit CO_2 absorption efficiency along the tower, scale-up of the spray tower is limited. To address this, future work should investigate modifications to the orifice plate design aimed at preserving droplet uniformity beyond the upper region of the tower. Design strategies should specifically account for the uneven droplet deceleration. Additionally, incorporating liquid recycling appears essential to reduce the required tower height. Therefore, the subsequent section places emphasis on evaluating operability with liquid recycling.

4.2. Operability assessment of gas-liquid reactive precipitation

This study aims to demonstrate the stable operation of gas-liquid reactive precipitation in a spray tower using the $GBIG/GBIGH_2(HCO_3)_2 \cdot 2H_2O$ and the $Ba(OH)_2/BaCO_3$ systems. Visual observations of the sump during batch experiments are provided in Fig. 10. The $GBIG/GBIGH_2(HCO_3)_2 \cdot 2H_2O$ system generates solids that remain suspended within the liquid phase for extended periods before gradually settling. Additionally, the protonation of GBIG results in a visibly reduced solution color intensity. In contrast, the $Ba(OH)_2/BaCO_3$ system forms solid agglomerates that initially rise to

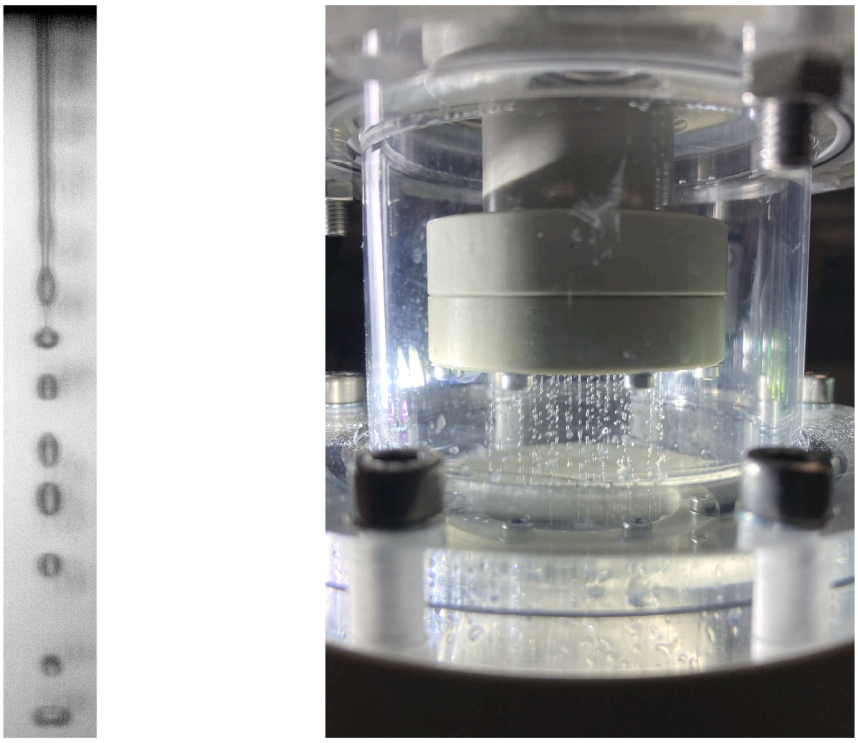

(a) Droplet formation. (b) Spray head.

Fig. 7. Liquid dispersion.

the liquid surface, followed by sedimentation to the sump bottom. Unlike the gradual precipitation observed with GBIG, the introduction of aqueous $Ba(OH)_2$ induces rapid solid formation. Notably, significant deposits of $BaCO_3$ accumulate on the inner wall of the spray tower just below the spray head (cf. Appendix I), a phenomenon not observed for $GBIGH_2(HCO_3)_2 \cdot 2H_2O$ solids.

Throughout the batch experiments, suspension is withdrawn from just beneath the liquid surface of the sump. Although some solids are entrained and transported upward into the spray head, this does not result in any observable scaling or clogging of the orifices. Upon disassembling the spray head, only traces of $GBIGH_2(HCO_3)_2 \cdot 2H_2O$ or $BaCO_3$ are found on the orifice plate. This suggests that the suspended particles are considerably smaller than the 150 µm orifice openings and are able to pass through the perforations unobstructed.

Although they exhibit distinct behaviors, both systems demonstrate operability in single-pass and batch mode.

Following CO_2 capture, the precipitated solids are examined via PXRD (cf. Fig. 11). The experimental diffractograms of $GBIGH_2(HCO_3)_2 \cdot 2H_2O$ and $BaCO_3$ closely match their simulated counterparts, confirming their identity.

4.3. Performance evaluation

Building upon the qualitative insights, this section analyzes the performance metrics (cf. Section 3.1) using the derived species distribution (cf. Section 3.6) to assess the spray-based gas-liquid reactive precipitation. Additionally, the measured pH is evaluated.

In the batch experiments, the absorption equilibrium is governed by the component system, the partial pressure of CO_2 and the temperature. The overall kinetics examined in single-pass mode are additionally shaped by the spray tower's geometry and operating conditions. Thus, the performance metrics of the single-pass experiments are evaluated with respect to feed stoichiometry ($\dot{n}_{\mathrm{gas,in,CO_2}} \dot{n}^{-1}_{\mathrm{liquid,in,OH^-_{(eq)}}}$). Horizontal lines in the data plots indicate the equilibrium values/maximum CO_2 capture capacity obtained from batch trials.

Fig. 12 depicts the experimental results. The CO_2 recovery drops as the $\dot{n}_{\mathrm{gas,in,CO_2}} \dot{n}^{-1}_{\mathrm{liquid,in,OH^-_{(eq)}}}$-ratio rises due to the relative decrease in absorbent capacity (cf. Fig. 12(a)). In Fig. 12(b), the CO_2 capture efficiency exhibits values of approximately 0.5 or 1, corresponding to the predominant formation of CO_3^{2-} and HCO_3^-, which consume two and one OH^- per CO_2 absorbed, respectively. The $Ba(OH)_2/BaCO_3$ and NaOH systems demonstrate comparable recoveries in the single-pass experiments. Analogously, both achieve a capture efficiency close to 0.5, which suggests a build-up of CO_3^{2-} across the explored stoichiometric range. This indicates that $BaCO_3$ precipitation does not impose a kinetic constraint on the overall process. Instead, the hydroxylation reaction (R5) appears to govern process kinetics. The GBIG/$GBIGH_2(HCO_3)_2 \cdot 2H_2O$ system exhibits lower recovery performance. Aqueous GBIG induces HCO_3^- accumulation ($\psi \approx 1$) as CO_2 hydration (Reaction (R1)) including consecutive dissociation (Reaction (R2)) is the dominant mechanism. As discussed in Section 2.1, hydration exhibits slower reaction rates than hydroxylation at elevated pH. Despite this kinetic limitation, the GBIG/$GBIGH_2(HCO_3)_2 \cdot 2H_2O$ system ultimately offers a considerably greater maximum CO_2 capture capacity per $OH^-_{(eq)}$ than the $Ba(OH)_2/BaCO_3$ system, owing to the dominant HCO_3^- formation. In contrast, the NaOH system demonstrates the ability to convert nearly all initially formed CO_3^{2-} into HCO_3^- as the absorption equilibrium is approached, resulting in a similar capture capacity as the bis(iminoguanidine) system.

In Fig. 12(c), the $OH^-_{(eq)}$ utilization efficiency is depicted. At absorption equilibrium, all systems achieve full $OH^-_{(eq)}$ utilization. However, the kinetic limitation of the GBIG/$GBIGH_2(HCO_3)_2 \cdot 2H_2O$ system becomes evident during the single-pass experiments, as it leaves a substantial fraction of its $OH^-_{(eq)}$ capacity unused. While the GBIG/$GBIGH_2(HCO_3)_2 \cdot 2H_2O$ system consistently performs below 30 % utilization across a wide stoichiometric range, the $Ba(OH)_2/BaCO_3$

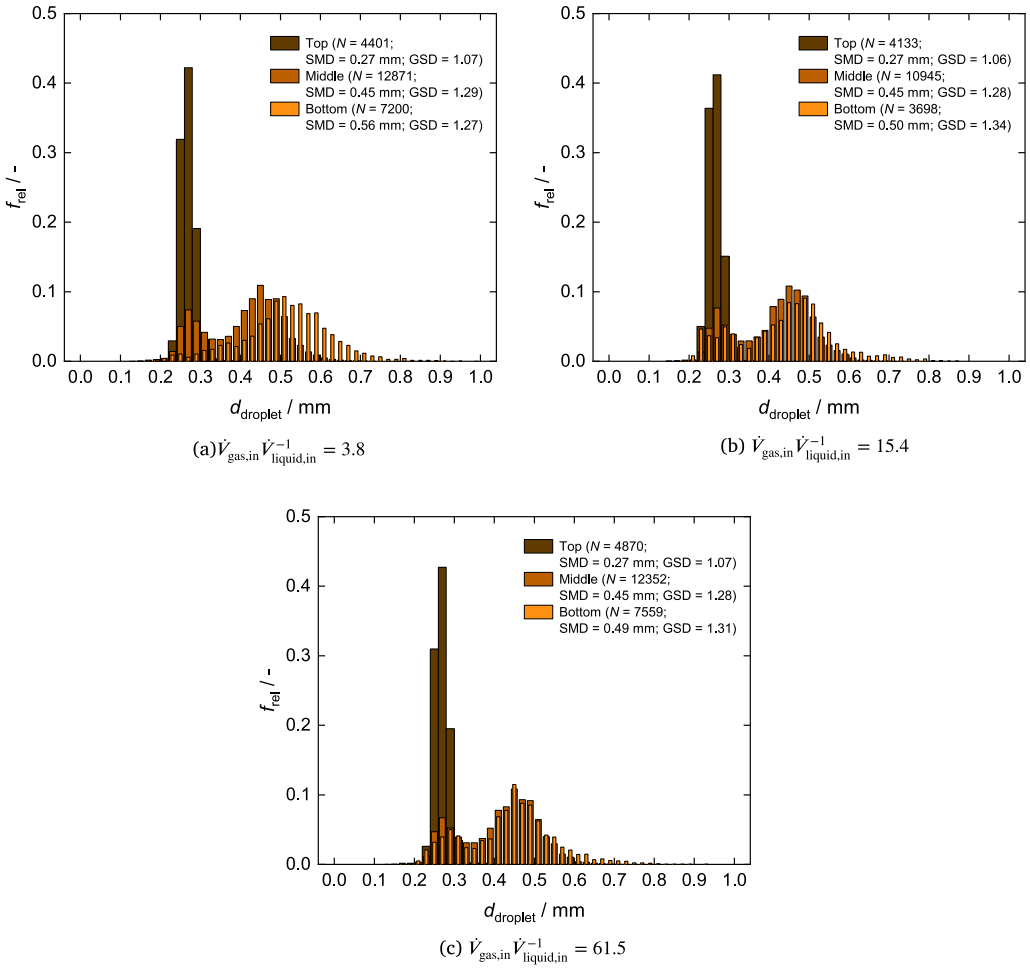

Fig. 8. Droplet size distribution.

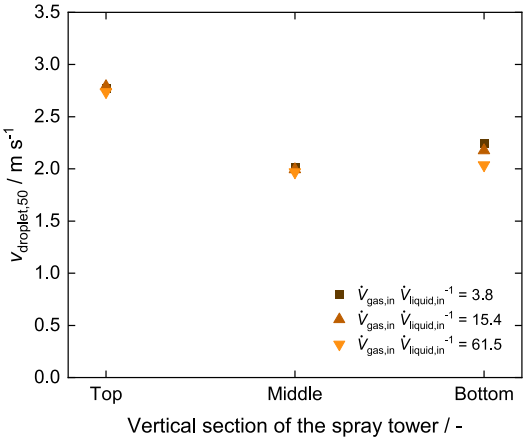

Fig. 9. Median droplet velocity.

and NaOH systems achieve high utilization of their $OH^-_{(eq)}$ capacity, which only decreases under substoichiometric feeding conditions. Notably, raising the $\dot{n}_{gas,in,CO_2}\dot{n}^{-1}_{liquid,in,OH^-_{(eq)}}$-ratio beyond two generates only marginal increases in $\omega_{OH^-_{(eq)}}$ (and also ψ). In contrast, a more pronounced improvement is expected from extending the liquid residence time or increasing the mass transfer area, which is consistent with the conclusions drawn from the analysis of droplet size and velocity (cf. Section 4.1). Accordingly, substantial recycling of the liquid phase appears inevitable. Furthermore, the addition of kinetic promoters (e.g., methyl amino propylamine Knuutila et al., 2009) to the electrolyte should be considered in future studies.

A deeper understanding of the process characteristics can be obtained by analyzing its pH sensitivity (cf. Fig. 12(d)). Generally, the $\dot{n}_{gas,in,CO_2}\dot{n}^{-1}_{liquid,in,OH^-_{(eq)}}$-ratio significantly influences the system's pH only under substoichiometric conditions, while its effect is marginal at superstoichiometric feeding. During the single-pass experiments, the NaOH system stabilizes at a pH near pK_{R3}, indicating the conversion of CO_3^{2-} to HCO_3^-. At equilibrium, the pH drops slightly below eight. In comparison, the $Ba(OH)_2/BaCO_3$ system transitions to a neutral, nearly terminal pH even at low $\dot{n}_{gas,in,CO_2}\dot{n}^{-1}_{liquid,in,OH^-_{(eq)}}$-ratios. This behavior can be attributed to the low concentration of CO_3^{2-} in the solution, which results in a reduced buffering capacity. By contrast, the $GBIG/GBIGH_2(HCO_3)_2 \cdot 2H_2O$ system maintains a moderate pH throughout operation, a consequence of its comparatively low pK values (cf. Reactions (R6) and (R7)). Thus, the kinetic limitation of the $GBIG/GBIGH_2(HCO_3)_2 \cdot 2H_2O$ system originates from a low pH, which results in the dominance of the kinetically slower hydration reaction and, consequently, a reduced absorption rate.

Beyond the data shown here, additional information on CO_2 volume fraction in the outlet, temperature, gauge pressure and molar isentropic work for pumping and compression can be found in the supplementary material (cf. Appendix J).

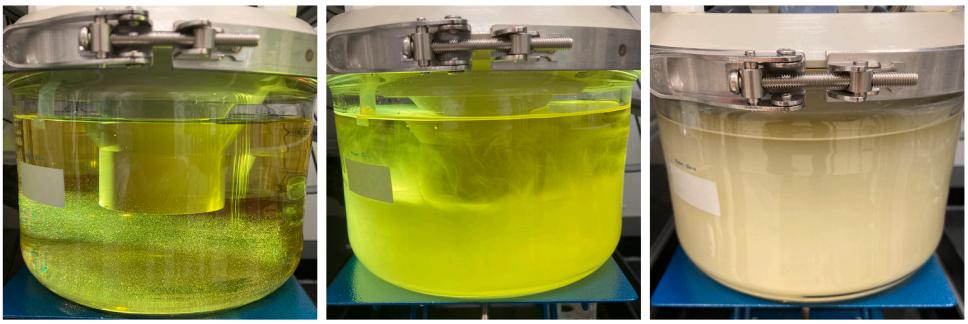

(a) GBIG/$GBIGH_2(HCO_3)_2 \cdot 2H_2O$ system

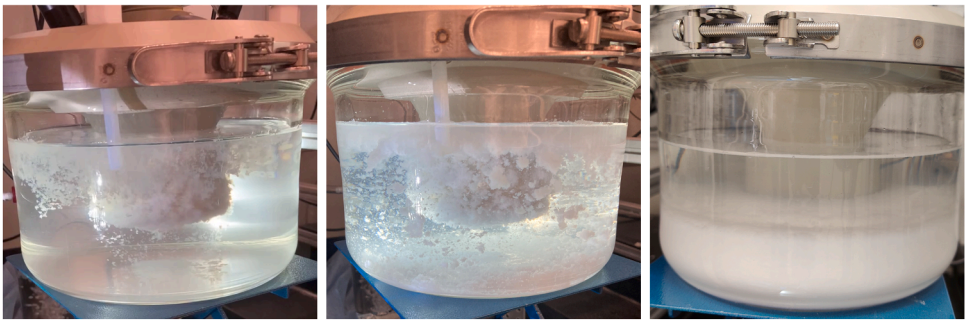

(b) $Ba(OH)_2/BaCO_3$ system

Fig. 10. Progressive solid accumulation in the sump over the course of the batch experiments.

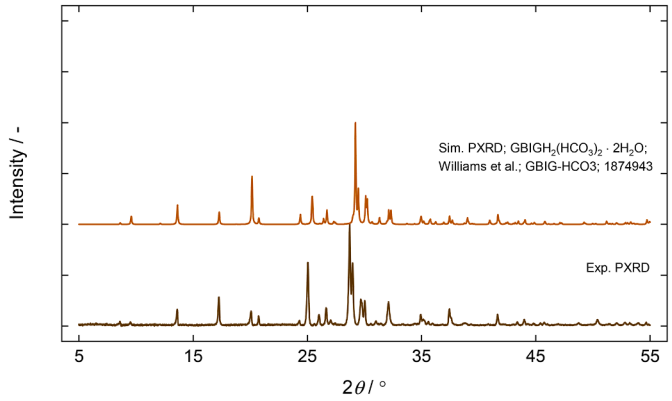

(a) $GBIGH_2(HCO_3)_2 \cdot 2H_2O$ (Component structure from Williams et al. (2019))

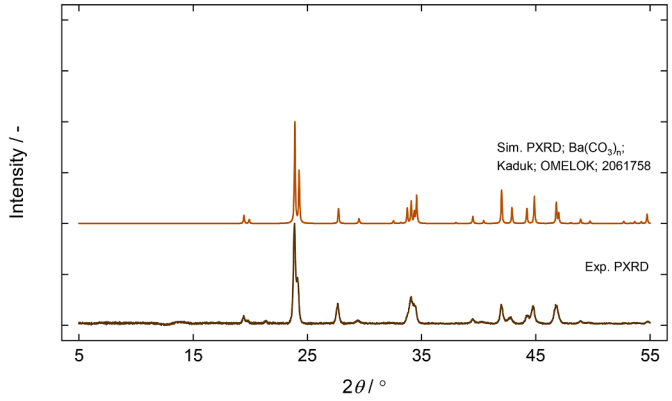

(b) $BaCO_3$ (Component structure from Kaduk (2021))

Fig. 11. PXRD patterns of precipitates (Kaduk, 2021).

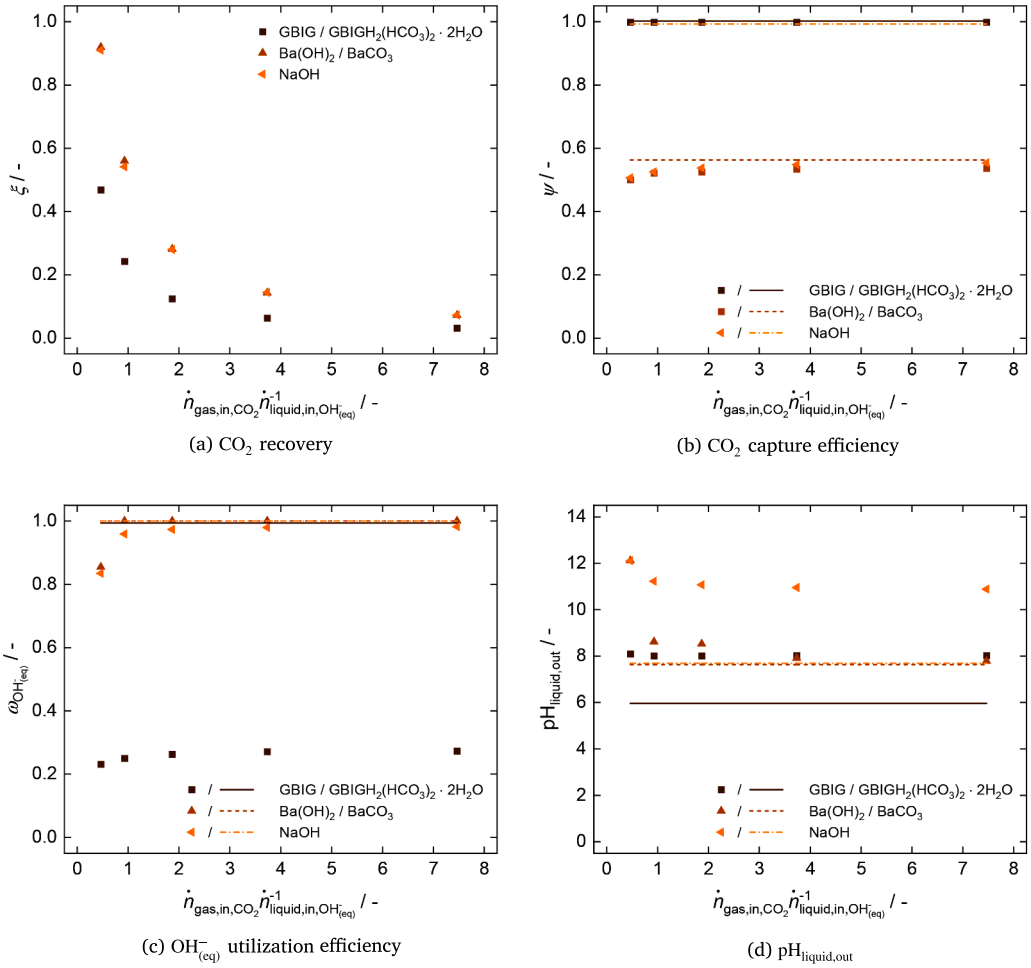

(a) CO_2 recovery

(b) CO_2 capture efficiency

(c) $OH^-_{(eq)}$ utilization efficiency

(d) $pH_{liquid,out}$

Fig. 12. Sensitivity analysis of spray tower performance with respect to $\dot{n}_{gas,in,CO_2}\dot{n}^{-1}_{liquid,in,OH^-_{(eq)}}$.

5. Conclusions

This work presents the first explicit investigation of spray tower operability in the context of gas-liquid reactive precipitation for CO_2 capture. Liquid jet disintegration is successfully tuned to a Rayleigh breakup regime, yielding a narrowly distributed droplet size spectrum at the top of the gas-liquid contacting zone. However, in contrast to the literature (Cho et al., 2018), a bimodal droplet size distribution emerges, accompanied by a noticeably higher SMD. This shift is presumably driven by frequent collisions among droplets of comparable size, potentially triggered by their uneven deceleration after the jet breakup. Such spatial non-uniformities in droplet behavior impede CO_2 absorption performance along the tower, thereby limiting the feasible scale-up of the tower height. Consequently, circulating a substantial fraction of the liquid phase may become essential to limit the overall height requirement.

This study further demonstrates the continuous operability of the spray tower as gas-liquid reactive precipitator in single-pass and batch mode. During solution recycling, small solid fractions are carried to the top of the tower. Nevertheless, no evidence of scaling or clogging at the orifice plate is detected, indicating that the precipitated solids are significantly smaller than the orifice diameter.

Ultimately, we compare the HCO_3^--precipitating GBIG system with a CO_3^{2-}-precipitating ($Ba(OH)_2/BaCO_3$) and a non-precipitating system (NaOH) using the pilot-scale spray tower. While the NaOH and $Ba(OH)_2/BaCO_3$ systems achieve comparable CO_2 recovery and $OH^-_{(eq)}$ utilization efficiency in the single-pass experiments, the GBIG/$GBIGH_2(HCO_3)_2 \cdot 2H_2O$ system consistently attains lower values. The kinetic limitation originates from the system's pH. CO_2 absorption in the NaOH and $Ba(OH)_2/BaCO_3$ systems is initially driven by the hydroxylation reaction (R5), which is kinetically superior at elevated pH. In contrast, the GBIG/$GBIGH_2(HCO_3)_2 \cdot 2H_2O$ system absorbs CO_2 entirely at moderate pH, where the hydration reaction (R1) is the dominating mechanism and kinetically inferior. However, the GBIG/$GBIGH_2(HCO_3)_2 \cdot 2H_2O$ and NaOH systems achieve significantly higher maximum CO_2 capture efficiencies compared to the $Ba(OH)_2/BaCO_3$ system, owing to the predominant accumulation of HCO_3^- per $OH^-_{(eq)}$. Generally, CO_2 recovery and $OH^-_{(eq)}$ utilization efficiency are most sensitive during substoichiometric feeding conditions. Exceeding a $\dot{n}_{gas,in,CO_2}\dot{n}^{-1}_{liquid,in,OH^-_{(eq)}}$-ratio of two yields only marginal changes in performance metrics. Increasing the liquid residence time, e.g., through liquid recycling, is believed to have a more pronounced effect, which is in accordance with the conclusion obtained from droplet size and velocity analysis.

The results warrant further research into spray-based gas-liquid reactive precipitation for CO_2 capture, with absorption kinetics and $OH^-_{(eq)}$ capacity identified as the dominant challenges. To address these topics, improvements in spray head design and electrolyte engineering are inevitable. Enhancing spatial uniformity within the tower through orifice/nozzle design modifications is essential to reduce tower height and improve scalability. In contrast, electrolyte engineering exhibits

multiple levers. Aqueous solutions can only dissolve small amounts of GBIG, thereby substantially limiting the cyclic capacity. Hence, the design of tailored analogs holds particular significance. In addition, industrial CO_2 capture is rarely performed without kinetic promoters. Consequently, their integration should be considered.

Beyond their use in pH-T swing systems, future studies may also investigate the suitability of phase-change absorbents for combined operation with electrochemical pH swing approaches.

CRediT authorship contribution statement

Robert Kiefel: Writing – review & editing, Writing – original draft, Supervision, Methodology, Investigation, Formal analysis, Conceptualization; **Jonas Görtz:** Methodology, Formal analysis, Writing – review & editing; **Jan Haß:** Methodology, Formal analysis, Writing – review & editing; **Julius Walorski:** Writing – review & editing, Methodology, Investigation, Formal analysis; **Falk Zimmer:** Writing – review & editing, Methodology, Investigation; **Andreas Jupke:** Writing – review & editing, Supervision, Resources, Project administration, Funding acquisition.

Declaration of competing interest

The authors declare that they have no known competing financial interests or personal relationships that could have appeared to influence the work reported in this paper.

Acknowledgements

The authors gratefully acknowledge the financial support of “ZeTA” within the framework of the research program “Modellregion, BioRevierPLUS: InBio, Innovationscluster Integrierte Bioraffinerie, TP2” (grant numbers: 031B1135B/031B1135BX), funded by the Federal Ministry of Education and Research (BMBF).

PXRD measurements were kindly provided by the research group of Prof. Ullrich Englert (RWTH Aachen University, Institute of Inorganic Chemistry, Crystallography and Structural Chemistry) and are gratefully acknowledged.

Additionally, the authors would like to thank Christoph Kiefel for his support with the schematic illustration of the breakup regime types.

Supplementary material

Supplementary material associated with this article can be found in the online version at 10.1016/j.ccst.2025.100509

References

Adamczyk, K., Prémont-Schwarz, M., Pines, D., Pines, E., Nibbering, E. T.J., 2009. Real-time observation of carbonic acid formation in aqueous solution. Science 326 (5960), 1690–1694. https://doi.org/10.1126/science.1180060

Aroonwilas, A., Tontiwachwuthikul, P., 1997. High-efficiency structured packing for CO_2 separation using 2-amino-2-methyl-1-propanol (AMP). Sep. Purif. Technol. 12 (1), 67–79. https://doi.org/10.1016/S1383-5866(97)00037-3

Baciocchi, R., Storti, G., Mazzotti, M., 2006. Process design and energy requirements for the capture of carbon dioxide from air. Chem. Eng. Process. 45 (12), 1047–1058. https://doi.org/10.1016/j.cep.2006.03.015

Bandyopadhyay, A., Biswas, M.N., 2007. Modeling of SO_2 scrubbing in spray towers. Sci. Total Environ. 383 (1–3), 25–40. https://doi.org/10.1016/j.scitotenv.2007.04.024

Buecker, B., 2008. Important concepts of wet-limestone flue gas desulfurization. In: Proceedings of the ASME 2008 Power Conference, pp. 91–98. https://doi.org/10.1115/POWER2008-60064

Chen, P.C., Huang, C.F., Chen, H.-W., Yang, M.-W., Tsao, C.-M., 2014a. Capture of CO_2 from coal-fired power plant with NaOH solution in a continuous pilot-scale bubble-column scrubber. Energy Proc. 61, 1660–1664. https://doi.org/10.1016/j.egypro.2014.12.186

Chen, P.-C., Kou, K.L., Tai, H.K., Jin, S.L., Lye, C.L., Lin, C.Y., 2002. Removal of carbon dioxide by reactive crystallization in a scrubber-kinetics of barium carbonate crystals. J. Cryst. Growth 237, 2166–2171. https://doi.org/10.1016/S0022-0248(01)02260-6

Chen, P.-C., Shi, W., Du, R., Chen, V., 2008. Scrubbing of CO_2 greenhouse gases, accompanied by precipitation in a continuous bubble-column scrubber. Indus. Eng. Chem. Res. 47 (16), 6336–6343. https://doi.org/10.1021/ie070324x

Chen, P.-C., Shi, W., Du, R., Chen, V., 2014b. Crystallization kinetics of barium carbonate crystals in a lab-scale bubble-column scrubber. J. Taiwan Inst. Chem. Eng. 45 (5), 2418–2426. https://doi.org/10.1016/j.jtice.2014.04.009

Chen, P.C., Yu, S.C., 2018. CO_2 Capture and crystallization of ammonia bicarbonate in a lab-scale scrubber. Crystals 8 (1), 39. https://doi.org/10.3390/cryst8010039

Chen, P.C., Zhuo, S.H., 2020. CO_2 capture in a bubble-column scrubber using $MEA/CaCl_2/H_2O$ solution–absorption and precipitation. Crystals 10 (8), 694. https://doi.org/10.3390/cryst10080694

Cho, M., Lee, S., Choi, M., Lee, J.W., 2018. Novel spray tower for CO_2 capture using uniform spray of monosized absorbent droplets. Indus. Eng. Chem. Res. 57 (8), 3065–3075. https://doi.org/10.1021/acs.iecr.7b05309

Crovetto, R., 1991. Evaluation of solubility data of the system CO_2–H_2O from 273 k to the critical point of water. J. Phys. Chem. Ref. Data 20 (3), 575–589. https://doi.org/10.1063/1.555905

Custelcean, R., 2021. Direct air capture of CO_2 via crystal engineering. Chem. Sci. 12 (38), 12518–12528. https://doi.org/10.1039/d1sc04097a

Custelcean, R., Williams, N.J., Wang, X., Garrabrant, K.A., Martin, H.J., Kidder, M.K., Ivanov, A.S., Bryantsev, V.S., 2020. Dialing in direct air capture of CO_2 by crystal engineering of bisiminoguanidines. ChemSusChem 13 (23), 6381–6390. https://doi.org/10.1002/cssc.202001114

Darde, V., Thomsen, K., van Well, W. J.M., Stenby, E.H., 2009. Chilled ammonia process for CO_2 capture. Energy Proc. 1 (1), 1035–1042. https://doi.org/10.1016/j.egypro.2009.01.137

Fosbøl, P.L., Gaspar, J., Ehlers, S., Kather, A., Briot, P., Nienoord, M., Khakharia, P., Le Moullec, Y., Berglihn, O.T., Kvamsdal, H., 2014. Benchmarking and comparing first and second generation post combustion CO_2 capture technologies. Energy Proc. 63, 27–44. https://doi.org/10.1016/j.egypro.2014.11.004

Garrabrant, K.A., Williams, N.J., Holguin, E., Brethomé, F.M., Tsouris, C., Custelcean, R., 2019. Energy-efficient CO_2 capture from flue gas by absorption with amino acids and crystallization with a bis-iminoguanidine. Indus. Eng. Chem. Res. 58 (24), 10510–10515. https://doi.org/10.1021/acs.iecr.9b00954

Gmehling, J., Kleiber, M., Kolbe, B., Rarey, J., 2019. Chemical Thermodynamics for Process Simulation. John Wiley & Sons. ISBN 978-3-527-34325-6.

Görtz, J., Seiler, J., Jupke, A., 2024a. Bubble up: tracking down the vertical velocity of oxygen bubbles in parallel plate electrolyzers using CNN. Int. J. Multiphase Flow 177, 104849. https://doi.org/10.1016/j.ijmultiphaseflow.2024.104849

Görtz, J., Seiler, J., Kolmer, P., Jupke, A., 2024b. Raising the curtain: bubble size measurement inside parallel plate electrolyzers. Chem. Eng. Sci. 286, 119550. https://doi.org/10.1016/j.ces.2023.119550

Green, D. W.a., Southard, M.Z., 2019. Perry’s Chemical Engineers’ Handbook, 9th ed.. McGraw-Hill Education. ISBN 978-0-071-83408-7.

van der Ham, L.V., Goetheer, E., Fernandez, E.S., Abu-Zahra, M., Vlugt, T., 2016. Precipitating amino acid solutions. In: Absorption-Based Post-combustion Capture of Carbon Dioxide. Elsevier. chapter 5, pp. 103–119. https://doi.org/10.1016/B978-0-08-100514-9.00005-6

Harned, H.S., Davis Jr , R., 1943. The ionization constant of carbonic acid in water and the solubility of carbon dioxide in water and aqueous salt solutions from 0 to 50°. J. Am. Chem. Soc. 65 (10), 2030–2037. https://doi.org/10.1021/ja01250a059

Harned, H.S., Scholes Jr , S.R., 1941. The ionization constant of HCO_3^- from 0 to 50°. J. Am. Chem. Soc. 63 (6), 1706–1709. https://doi.org/10.1021/ja01851a058

Hekmatmehr, H., Esmaeili, A., Pourmahdi, M., Atashrouz, S., Abedi, A., Abuswer, M.A., Nedeljkovic, D., Latifi, M., Farag, S., Mohaddespour, A., 2024. Carbon capture technologies: a review on technology readiness level. Fuel 363, 130898. https://doi.org/10.1016/j.fuel.2024.130898

Hill, G.A., 2006. Measurement of overall volumetric mass transfer coefficients for carbon dioxide in a well-mixed reactor using a pH probe. Indus. Eng. Chem. Res. 45 (16), 5796–5800. https://doi.org/10.1021/ie060242t

Ho, C., Sturtevant, J.M., 1963. The kinetics of the hydration of carbon dioxide at 25°. J. Biol. Chem. 238 (10), 3499–3501. https://doi.org/10.1016/S0021-9258(18)48695-4

Holterman, H.J., 2003. Kinetics and Evaporation of Water Drops in Air. IMAG. ISBN 978-9-054-06234-9.

Housecroft, C.E., Sharpe, A.G., 2012. Inorganic Chemistry. Pearson Education Limited. ISBN 978-0-273-74278-4.

IPCC, 2022. Climate Change 2022: Mitigation of Climate Change. Contribution of Working Group III to the Sixth Assessment Report of the Intergovernmental Panel on Climate Change. Cambridge University Press, Cambridge, UK and New York, NY, USA. https://doi.org/10.1017/9781009157926

Javed, K.H., Mahmud, T., Purba, E., 2010. The CO_2 capture performance of a high-intensity vortex spray scrubber. Chem. Eng. J. 162 (2), 448–456. https://doi.org/10.1016/j.cej.2010.03.038

Kaduk, J.A., 2021. Tribarium dicitrate pentahydrate, $[Ba_3(C_6H_5O_7)_2(H_2O)_4]\cdot H_2O$. Acta Crystallographica Section E 77 (3), 251–254. https://doi.org/10.1107/S2056989021001407

Keith, D.W., Holmes, G., Angelo, D.S., Heidel, K., 2018. A process for capturing CO_2 from the atmosphere. Joule 2 (8), 1573–1594. https://doi.org/10.1016/j.joule.2018.05.006

Khan, U., Ogbaga, C.C., Abiodun, O.-A.O., Adeleke, A.A., Ikubanni, P.P., Okoye, P.U., Okolie, J.A., 2023. Assessing absorption-based CO_2 capture: research progress and techno-economic assessment overview. Carbon Capture Sci. Technol. 8, 100125. https://doi.org/10.1016/j.ccst.2023.100125

Kim, H., Song, J., 2019. Jet breakup behavior of liquid carbon dioxide for coal transport applications. Exp. Therm Fluid Sci. 105, 349–355. https://doi.org/10.1016/j.expthermflusci.2019.04.015

Knuutila, H., Svendsen, H.F., Juliussen, O., 2009. Kinetics of carbonate based CO_2 capture systems. Energy Proc. 1 (1), 1011–1018. https://doi.org/10.1016/j.egypro.2009.01.134

Koller, M., Wappel, D., Trofaier, N., Gronald, G., 2011. Test results of CO_2 spray scrubbing with monoethanolamine. Energy Proc. 4, 1777–1782. https://doi.org/10.1016/j.egypro.2011.02.053

Kordac, M., Linek, V., 2008. Dynamic measurement of carbon dioxide volumetric mass transfer coefficient in a well-mixed reactor using a pH probe: analysis of the salt and supersaturation effects. Indus. Eng. Chem. Res. 47 (4), 1310–1317. https://doi.org/10.1021/ie0711776

Kozak, F., Petig, A., Morris, E., Rhudy, R., Thimsen, D., 2009. Chilled ammonia process for CO_2 capture. Energy Proc. 1 (1), 1419–1426. https://doi.org/10.1016/j.egypro.2009.01.186

Li, Z., Ji, X., Yang, Z., Lu, X., 2019. Experimental studies of air-blast atomization on the CO_2 capture with aqueous alkali solutions. Chin. J. Chem. Eng. 27 (10), 2390–2396. https://doi.org/10.1016/j.cjche.2019.01.021

Lide, D.R., 2004. CRC Handbook of Chemistry and Physics. 85. CRC press. ISBN 978-0-849-30485-9.

Lim, Y., Choi, M., Han, K., Yi, M., Lee, J., 2013. Performance characteristics of CO_2 capture using aqueous ammonia in a single-nozzle spray tower. Indus. Eng. Chem. Res. 52 (43), 15131–15137. https://doi.org/10.1021/ie401981u

Lin, S.P., Reitz, R.D., 1998. Drop and spray formation from a liquid jet. Annu. Rev. Fluid Mech. 30 (1), 85–105. https://doi.org/10.1146/annurev.fluid.30.1.85

Liu, H., Wang, C., Zhou, C., Song, L., Ma, K., Yue, H., 2024. Gas and slurry flow behaviors in a CO_2-mineralization spray tower reactor. AlChE J. 70 (4), e18329. https://doi.org/10.1002/aic.18329

Maharloo, D.G., Darvishi, A., Davand, R., Saidi, M., Rahimpour, M.R., 2017. Process intensification and environmental consideration of sodium bicarbonate production in an industrial soda ash bubble column reactor by CO_2 recycling. J. CO_2 Utiliz. 20, 318–327. https://doi.org/10.1016/j.jcou.2017.06.005

McCann, N., Phan, D., Wang, X., Conway, W., Burns, R., Attalla, M., Puxty, G., Maeder, M., 2009. Kinetics and mechanism of carbamate formation from $CO_{2(aq)}$, carbonate species, and monoethanolamine in aqueous solution. J. Phys. Chem. A 113 (17), 5022–5029. https://doi.org/10.1021/jp810564z

Mook, W.G., 2000. Environmental Isotopes in the Hydrological Cycle: Principles and Applications, V. I: Introduction; Theory, Methods, Review. Technical Report. International Atomic Energy Agency and United Nations Educational, Scientific and Cultural Organisation.

Mumford, K.A., Wu, Y., Smith, K.H., Stevens, G.W., 2015. Review of solvent based carbon-dioxide capture technologies. Front. Chem. Sci. Eng. 9, 125–141. https://doi.org/10.1007/s11705-015-1514-6

Ochedi, F.O., Yu, J., Yu, H., Liu, Y., Hussain, A., 2021. Carbon dioxide capture using liquid absorption methods: a review. Environ. Chem. Lett. 19, 77–109. https://doi.org/10.1007/s10311-020-01093-8

Onimisi, J.A., Ismail, R., Ariffin, K.S., Baharun, N., Hussin, H.B., 2016. A novel rapid mist spray technique for synthesis of single phase precipitated calcium carbonate using solid-liquid-gas process. Korean J. Chem. Eng. 33, 2756–2760. https://doi.org/10.1007/s11814-016-0093-7

Perry, R.J., Wood, B.R., Genovese, S., O'Brien, M.J., Westendorf, T., Meketa, M.L., Farnum, R., McDermott, J., Sultanova, I., Perry, T.M., Vipperla, R.-K., Wichmann, L.A., Enick, R.M., Hong, L., Tapriyal, D., 2012. CO_2 capture using phase-changing sorbents. Energy Fuels 26 (4), 2528–2538. https://doi.org/10.1021/ef300079w

Pinsent, B., Pearson, L., Roughton, F., 1956. The kinetics of combination of carbon dioxide with hydroxide ions. Trans. Faraday Soc. 52, 1512–1520. https://doi.org/10.1039/TF9565201512

Pinsent, B., Roughton, F., 1951. The kinetics of combination of carbon dioxide with water and hydroxide ions. Trans. Faraday Soc. 47, 263–269. https://doi.org/10.1039/TF9514700263

Pocker, Y., Bjorkquist, D.W., 1977. Stopped-flow studies of carbon dioxide hydration and bicarbonate dehydration in H_2O and D_2O. acid-base and metal ion catalysis. J. Am. Chem. Soc. 99 (20), 6537–6543. https://doi.org/10.1021/ja00462a012

Global Carbon Project, 2025. Global Carbon Atlas. Accessed 10 May 2025 https://globalcarbonatlas.org/emissions/carbon-emissions/.

Raksajati, A., Ho, M.T., Wiley, D.E., 2016. Understanding the impact of process design on the cost of CO_2 capture for precipitating solvent absorption. Indus. Eng. Chem. Res. 55 (7), 1980–1994. https://doi.org/10.1021/acs.iecr.5b03633

Sanchez-Fernandez, E., de Miguel Mercader, F., Misiak, K., Van Der Ham, L., Linders, M., Goetheer, E., 2013. New process concepts for CO_2 capture based on precipitating amino acids. Energy Proc. 37, 1160–1171. https://doi.org/10.1016/j.egypro.2013.05.213

Shim, J.-G., Lee, D.W., Lee, J.H., Kwak, N.-S., 2016. Experimental study on capture of carbon dioxide and production of sodium bicarbonate from sodium hydroxide. Environ. Eng. Res. 21 (3), 297–303. https://doi.org/10.4491/eer.2016.042

Sibirtsev, S., 2022. Mask R-CNN implementation for droplet detection in liquid multiphase systems. https://github.com/ssibirtsev/MRCNN-droplet-detection. GitHub repository.

Sibirtsev, S., Zhai, S., Jupke, A., 2024. Mask R-CNN based droplet detection in liquid–liquid systems, Part 3: model generalization for accurate processing performance independent of image quality. Chem. Eng. Res. Des. 202, 161–168. https://doi.org/10.1016/j.cherd.2023.12.005

Sibirtsev, S., Zhai, S., Neufang, M., Seiler, J., Jupke, A., 2023. Mask R-CNN based droplet detection in liquid–liquid systems, Part 2: methodology for determining training and image processing parameter values improving droplet detection accuracy. Chem. Eng. J. 473, 144826. https://doi.org/10.1016/j.cej.2023.144826

Sirs, J.A., 1958. Electrometric stopped flow measurements of rapid reactions in solution. Part 1.–conductivity measurements. Trans. Faraday Soc. 54, 201–206. https://doi.org/10.1039/TF9585400201

Smith, K.H., Harkin, T., Mumford, K., Kentish, S., Qader, A., Anderson, C., Hooper, B., Stevens, G.W., 2017. Outcomes from pilot plant trials of precipitating potassium carbonate solvent absorption for CO_2 capture from a brown coal fired power station in Australia. Fuel Process. Technol. 155, 252–260. https://doi.org/10.1016/j.fuproc.2016.08.008

Soli, A.L., Byrne, R.H., 2002. CO_2 system hydration and dehydration kinetics and the equilibrium CO_2/H_2CO_3 ratio in aqueous NaCl solution. Mar. Chem. 78 (2–3), 65–73. https://doi.org/10.1016/S0304-4203(02)00010-5

Spigarelli, B.P., Kawatra, S.K., 2013. Opportunities and challenges in carbon dioxide capture. J. CO_2 Utiliz. 1, 69–87. https://doi.org/10.1016/j.jcou.2013.03.002

Srivastava, R.K., Jozewicz, W., 2001. Flue gas desulfurization: the state of the art. J. Air & Waste Manag. Assoc. 51 (12), 1676–1688. https://doi.org/10.1080/10473289.2001.10464387

Stolaroff, J.K., Keith, D.W., Lowry, G.V., 2008. Carbon dioxide capture from atmospheric air using sodium hydroxide spray. Environ. Sci. Technol. 42 (8), 2728–2735. https://doi.org/10.1021/es702607w

Suñol, F., González-Cinca, R., 2015. Liquid jet breakup and subsequent droplet dynamics under normal gravity and in microgravity conditions. Phys. Fluids 27 (7). https://doi.org/10.1063/1.4927365

Tamura, K., Tsuge, H., 2006. Characteristics of multistage column crystallizer for gas–liquid reactive crystallization of calcium carbonate. Chem. Eng. Sci. 61 (17), 5818–5826. https://doi.org/10.1016/j.ces.2006.05.002

Tyler, E., 1933. XL. Instability of liquid jets. London Edinburgh Dublin Philos. Magaz. J. Sci. 16 (105), 504–518. https://doi.org/10.1080/14786443309462302

Van Hoeve, W., Gekle, S., Snoeijer, J.H., Versluis, M., Brenner, M.P., Lohse, D., 2010. Breakup of diminutive Rayleigh jets. Phys. Fluids 22 (12). https://doi.org/10.1063/1.3524533

Varma, S., Chen, P.-C., Unnikrishnan, G., 2011. Gas–liquid reactive crystallization for the synthesis of $CaCO_3$ nanocrystals. Mater. Chem. Phys. 126 (1–2), 232–236. https://doi.org/10.1016/j.matchemphys.2010.11.034

Vukasinovic, B., Smith, M.K., Glezer, A., 2004. Spray characterization during vibration-induced drop atomization. Phys. Fluids 16 (2), 306–316. https://doi.org/10.1063/1.1632907

Wang, C., Liu, M., Liu, H., Yang, Q., Zhou, C.-A., Song, L., Ma, K., Yue, H., 2025. Numerical analysis of CO_2 absorption characteristics in industrial flue gas mineralization spray tower reactor. Sep. Purif. Technol. 354, 129051. https://doi.org/10.1016/j.seppur.2024.129051

Wang, X., Conway, W., Burns, R., McCann, N., Maeder, M., 2010. Comprehensive study of the hydration and dehydration reactions of carbon dioxide in aqueous solution. J. Phys. Chem. A 114 (4), 1734–1740. https://doi.org/10.1021/jp909019u

Westendorf, T. E.P., Genovese, S.E., Grocela-Rocha, T., Perry, R.J., Wood, B.R., 2010. Carbon Dioxide Capture System and Methods of Capturing Carbon Dioxide. US patent application 8,709,367 B2, filed 30 July 2010

Williams, N.J., Seipp, C.A., Brethomé, F.M., Ma, Y.-Z., Ivanov, A.S., Bryantsev, V.S., Kidder, M.K., Martin, H.J., Holguin, E., Garrabrant, K.A., Custelcean, R., 2019. CO_2 Capture via crystalline hydrogen-bonded bicarbonate dimers. Chem 5 (3), 719–730. https://doi.org/10.1016/j.chempr.2018.12.025

Wu, X.-c., Li, C., Cao, J.-z., Zhang, Y.-x., Chen, L.-h., Gréhan, G., Cen, K.-f., 2018. In-situ characterization of gas-liquid precipitation reaction in a spray using rainbow refractometry. J. Zhejiang Univer. Sci. A 19 (1), 86–94. https://doi.org/10.1631/jzus.A1700240

Zhang, S., Shen, Y., Wang, L., Chen, J., Lu, Y., 2019. Phase change solvents for post-combustion CO_2 capture: principle, advances, and challenges. Appl. Energy 239, 876–897. https://doi.org/10.1016/j.apenergy.2019.01.242

Zhang, Z., Li, Y., Zhang, W., Wang, J., Soltanian, M.R., Olabi, A.G., 2018. Effectiveness of amino acid salt solutions in capturing CO_2: a review. Renew. Sustain. Energy Rev. 98, 179–188. https://doi.org/10.1016/j.rser.2018.09.019

Zhu, J., Ye, S.-c., Bai, J., Wu, Z.-y., Liu, Z.-h., Yang, Y.-f., 2015. A concise algorithm for calculating absorption height in spray tower for wet limestone–gypsum flue gas desulfurization. Fuel Process. Technol. 129, 15–23. https://doi.org/10.1016/j.fuproc.2014.07.002